Int. J. Electrochem. Sci., 14 **(2019)** 4195 – 4205, doi: 10.20964/2019.05.07

International Journal of
ELECTROCHEMICAL
SCIENCE
www.electrochemsci.org

Formation of Highly Dispersed Ultrafine MnO_2 Nanoparticles on Nitrogen-doped Porous Carbon for Supercapacitor Applications

Xiaoxiao Du[1], *Qiong Chen*[2], *Cuili Xiang*[1,*], *Yongjin Zou*[1], *Fen Xu*[1], *Jingjing Xie*[3], *Lixian Sun*[1,*]

[1] Guangxi Key Laboratory of Information Materials, Guilin University of Electronic Technology, Guilin 541004, P.R. China
[2] The Fifth Electronic Research Institute of the Ministry of Industry and Information Technology, Guangzhou, 510610, China
[3] State Key Laboratory of Advanced Technology for Materials Synthesis and Processing, Wuhan University of Technology, Wuhan, 430070, China
[*]E-mail: xiangcuili@guet.edu.cn; sunlx@guet.edu.cn

Received: 9 January 2019 / *Accepted:* 31 January 2019 / *Published:* 10 April 2019

Formation of transition metal oxide doped nanostructures with high surface area is highly desirable for electrochemical applications. Here, ultrafine MnO_2 nanoparticles dispersed nitrogen-doped porous carbons (MnO_2/N-C) was synthesized using chitosan and $Mn(NO_3)_2$ as precursor. The MnO_2/N-C demonstrates outstanding supercapacitive properties and great potential for real-world applications. The capacitance of the nanocomposite is as high as 340.1 F g^{-1} (1 A g^{-1}) in 1 M KOH solution. The MnO_2/N-C also shows high-rate capability, retaining a specific capacitance of 270.2 F g^{-1} at 10 A g^{-1}. The large specific surface area and highly-dispersed MnO_2 combined with its unique structural advantages, make it a very promising electrode material for energy storage devices.

Keywords: MnO_2; Supercapacitor; N-doped; Highly dispersed; Nanocomposite

1. INTRODUCTION

Supercapacitor is an attractive energy storage device, which possesses high power density, short charge-discharging time, light weight and long-cycle life [1, 2]. There are two types of supercapacitor according the charge storage mechanisms. One is electrical double layer capacitor (EDLC). The charges can be stored on the surface of the electrode materials electrostatically. Therefore, materials for EDLC must have high surface area, which can provide effective sites for the charge accumulation. Carbonaceous materials are widely used as the electrode materials for EDLC [3, 4]. The other type of supercapacitor is pseudocapacitor. The electrical energy is stored through the reversible Faradaic reactions. Transition metal oxides and conducting polymers are well-known materials for electrochemical active materials [5-9], which are widely used in pseudocapacitors. However, both types of supercapacitor have their advantages and disadvantages. For instance, EDLC has outstanding stability, high power density and long cycle life owing to the good stability and conductivity of carbon materials. However, EDLC has low capacitance, usually less than 300 F g^{-1}. While the pseudocapacitors have extremely high capacitance (more than 1000 F g^{-1}), however, the stability are poor because of the low conductivity and the volume change of the active materials. Therefore, combination of the EDLC and pseudocapacitors has become the favorite way to improve the electrochemical performance of the supercapacitors.

MnO_2, a widely used energy material, has excellent electrochemical activity and stability [10-12]. The theoretical capacitance of MnO_2 electrode is as high as 1370 F g^{-1}. Furthermore, MnO_2 based materials can work at neutral aqueous electrolyte, which reduced the corrosion of active materials [13]. Therefore, different nanostructures of MnO_2 including nanoparticles, nanowires, nanorods, nanourchins have been prepared. For instance, Bai et al. synthesized porous multidimensional MnO_2 via hydrothermal method, which demonstrated high supercapacitive property (311.52 F g^{-1} at 0.3 A g^{-1}) [14]. Feng et al. prepared free-standing MnO_2 nanoflowers. A high specific capacitance of 368.3 F g^{-1} was obtained at 0.2 A g^{-1} [15]. By simple template-assisted hydrothermal method, Wang et al. prepared bowl-like MnO_2 nanosheets. The resulting MnO_2 nanosheets exhibit a high specific (379 F g^{-1} at 0.5 A g^{-1}) [16]. Though the electrochemical performance of MnO_2 can be tuned by manipulating its structure, the capacitance of MnO_2 is still much lower than the theoretical value owing to its poor electrical conductivity and low structural stability. To address this problem, the MnO_2 nanoparticles have to be anchored on the carbon-based materials [17-20]. However, dispersion of ultrafine MnO_2 nanoparticles on the surface of carbon materials is still challenging due to the aggregation of the nanoparticles [21-23].

Herein, a composite of highly dispersed MnO_2 nanoparticles anchored nitrogen-doped porous carbon was facilely prepared by carbonization of the mixture of chitosan and $Mn(NO_3)_2$. Compared with previous approaches, the proposed method not only greatly enhances contactable area of MnO_2 with carbon substrate, but also effectively improves the stability of active materials. It provides a stable, scalable, and cost-effective route to fabricate MnO_2/N-C nanocomposite, which is important for energy storage devices.

2. MATERIALS AND METHODS

2.1. Synthesis of MnO_2/N-C

Chitosan and $Mn(NO_3)_2$ were employed as precursors. Briefly, 1 g of chitosan powder and 1 g of acetic acid was added to 100 mL of deionized water and stirred vigorously, followed by the addition of 0.01 g of $Mn(NO_3)_2$ under stirring. Then the solvent was evaporated at 60 ºC in a vacuum for 24 h. The solid was collected and carbonized at 800 ºC for 3 h under Ar flow to obtain the final MnO_2/N-C. For comparison, the chitosan derived carbon was prepared under the identical condition and denoted as

Chit-C.

2.2. Characterization

The morphology of the resulting samples was examined by scanning electron microscopy (SEM, Quanta 200) and (high-resolution) transmission electron microscopy ((HR)TEM, Tecnai F20, FEI). The crystallographic properties of the samples were measured on an X-ray diffractometer (1820 Philips) using Cu Ka radiation between 5° and 80°. The chemical state of the elements in the samples was characterized by the X-ray photoelectron spectrometer (XPS, Thermo Fisher Scientific). N_2 adsorption/desorption measurements was determined by Brunauer–Emmett–Teller (BET) method using a Quantachrome Autosorb-iQ2 Automated gas sorption system at 77 K.

2.3. Electrochemical tests

All electrochemical studies were conducted on a CHI660E electrochemical workstation (Shanghai Chenhua Co., China) in 1 M KOH aqueous solution. The working electrodes were prepared using MnO_2/N-C as active material according our previous work [24]. An Ag/AgCl electrode was used as the reference electrode, and a platinum foil acted as the counter electrode. The specific capacitance was calculated based on established equations in the literature [24].

3. RESULTS AND DISCUSSION

3.1. Characteristics of composite samples

The crystal structures of the prepared MnO_2/N-C and Chit-C were investigated using XRD technique. As shown in Figure 1, the diffraction pattern of MnO_2/N-C consists of peaks located at 35.0° 40.6°, 58.8° can be indexed to (101), (200), (211) of MnO_2 (PDF No. 04-0591). Sharp diffraction peaks of MnO_2 indicate the phase purity of the synthesized nanoparticles is good [25]. The broad diffraction peak centered at 42.9° in the sample of Chit-C is indexed to (100) planes of amorphous carbon [26-29]. The XRD results indicate that manganese oxide is MnO_2.

The morphologies of the sample MnO_2/N-C and Chit-C were characterized by SEM. Figure 2a shows the SEM image of Chit-C. The Chit-C only shows smooth surface, while the images of MnO_2/N-C demonstrate porous structure (Figure 2b). From the magnified images of MnO_2/N-C, it can be observed that the carbon substrate was covered with t high density of MnO_2 nanoparticles (Figure 2c,d).

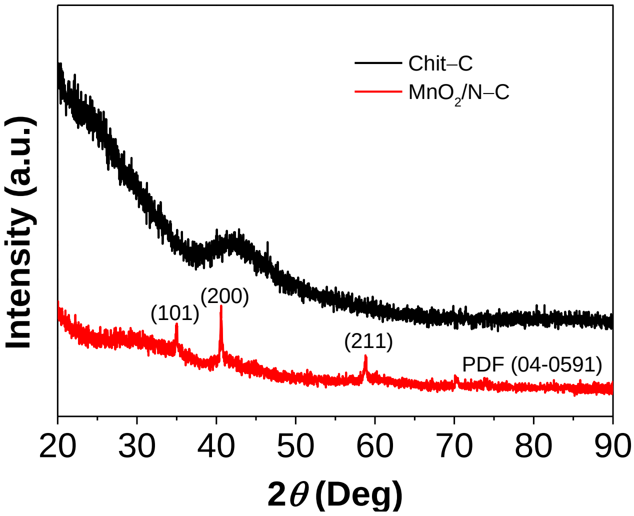

Figure 1. XRD pattern of the as-synthesized MnO_2/N-C and Chit-C.

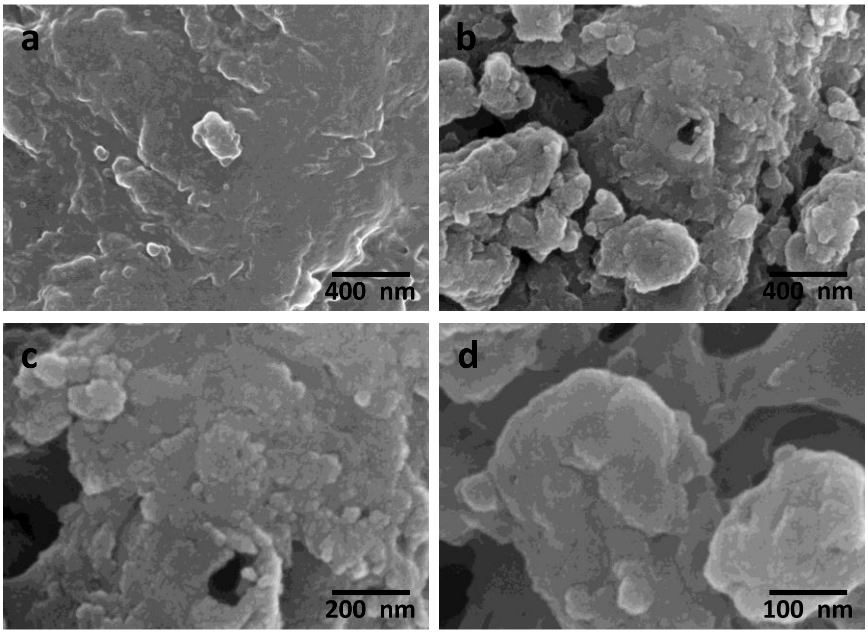

Figure 2. SEM images of Chit-C (a) and MnO_2/N-C (b,c,d).

The microstructure of MnO_2/N-C was further studied by TEM. As shown in Figure 3a, the porous structure of MnO_2/N-C was further confirmed. The ultrafine MnO_2 nanoparticles with an average diameter of 8 nm are well distributed on the carbon substrate (Figure 3b,c). No obvious aggregation was observed. Furthermore, from the HRTEM image of MnO_2/N-C, the carbon becomes graphitic due to the catalytic effect of Mn species (Figure 3d).

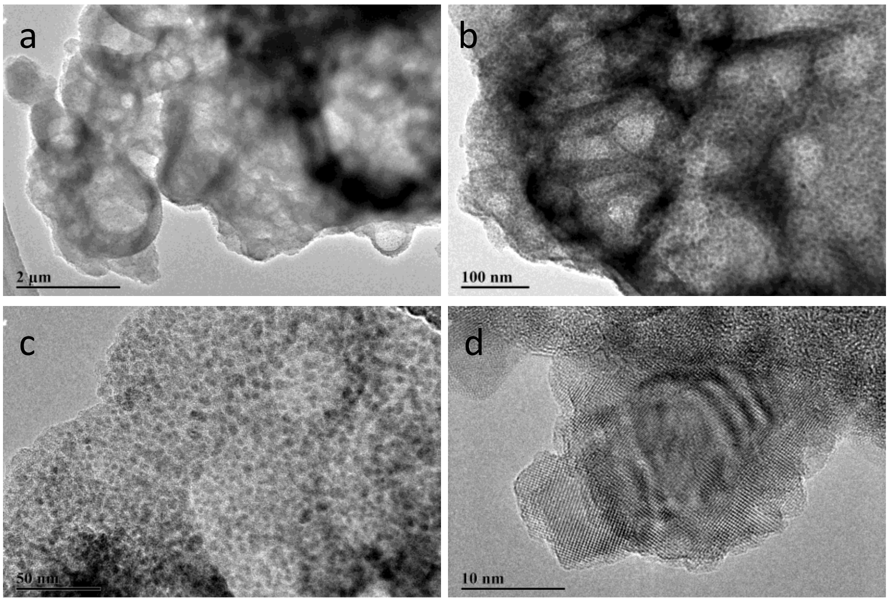

Figure 3. TEM images (a,b,c) and HRTEM (d) image of MnO_2/N-C.

Figure 4 shows the EDX elemental maps of C, Mn, O, and N in the sample of MnO_2/N-C. The map shapes of C, Mn and O are almost similar, suggesting the Mn and O are uniformly distributed on the surface of carbon matrix. N can also be found in the composite, which comes from the precursor chitosan.

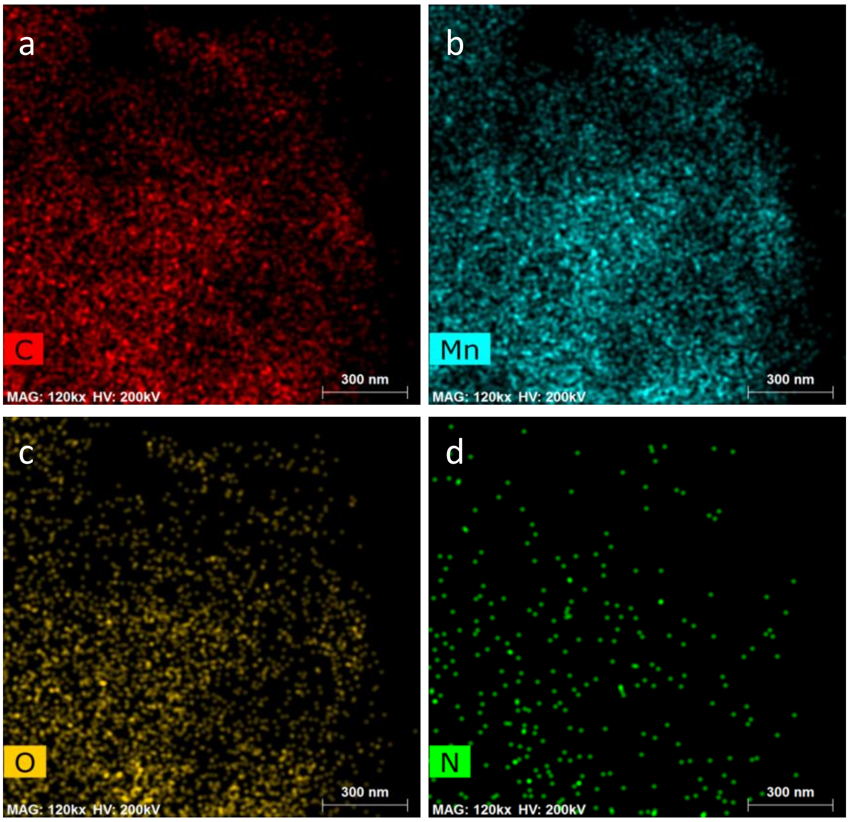

Figure 4. EDX elemental maps of C, Mn, O, and N in MnO_2/N-C.

The X-ray photoelectron spectroscopy (XPS) is a useful tool to study the chemical states of the elements [30-33]. The XPS data of sample MnO_2/N-C are shown in Figure 5. The C, Mn, O and N elements are confirmed in MnO_2/N-C (Figure 5a). Two peaks located at 641.5 eV and 653.4 eV in Mn 2p spectrum (Figure 5b), are identical with those of reported value of MnO_2 [34]. The Mn oxidation state can be identified from the Mn 3s core-level spectrum [34]. As shown in Figure 5c, the pin-orbit splitting energy of Mn 3s is 6.2 eV, indicating the existence of Mn^{2+}. The N 1s core-level spectrum of the MnO_2/N-C composite is shown in Figure 5d. It shows that nitrogen has three chemical states in the composite. The peak at 398.6 eV is indexed to the N–C bond, whereas the peaks at 399.6 and 404.8 eV peak can be assigned to N=C and N–O bonds, respectively [35].

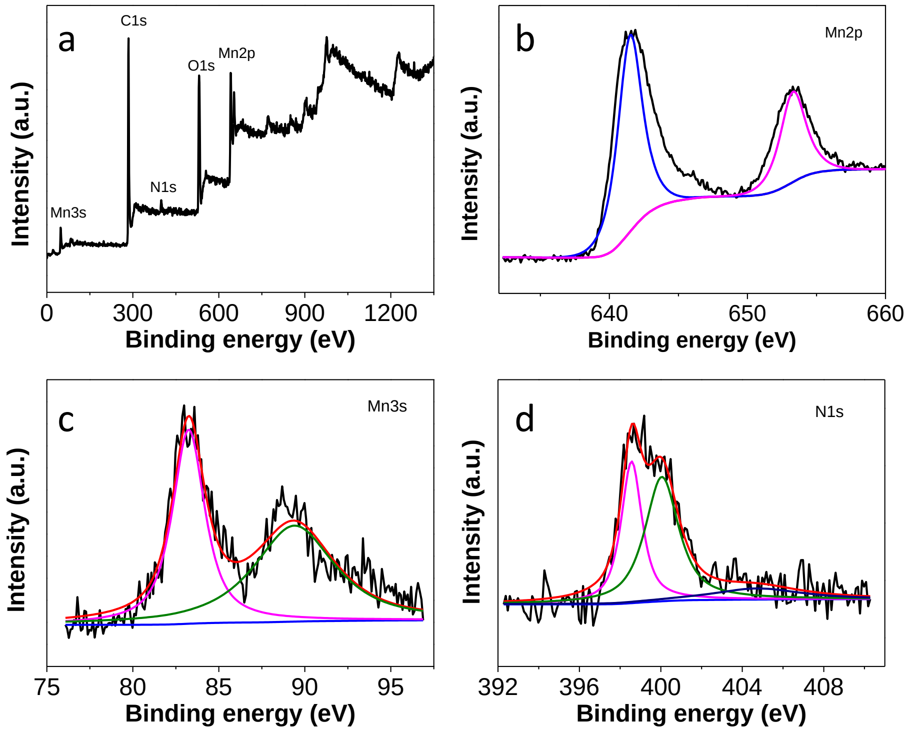

Figure 5. (a) Full XP spectrum of MnO_2/N-C and high-resolution spectra of the (b) Mn 2p, (c) Mn 3s, and (d) N 1s.

The specific surface area of the active materials is an important factor for the charge storage in supercapacitor. Figure 6a shows the isotherm of MnO_2/N-C, displaying a typical IV type curve, which indicates the existence of plenty of mesopores [36-38]. The BET surface area of MnO_2/N-C was calculated to be 104.7 $m^2 g^{-1}$, which is much higher surface area than reported transition metal doped carbon nanocomposite [10,11]. The MnO_2/N-C shows a narrow pore-size distribution with an average pore size of 4.1 nm (Figure 6b), which further confirms the existence of mesopores in MnO_2/N-C. The mesopores play important role of channels for accelerating the rapid transport of ions within MnO_2/N-C, which potentially provide an excellent platform for the charge storage [39-42].

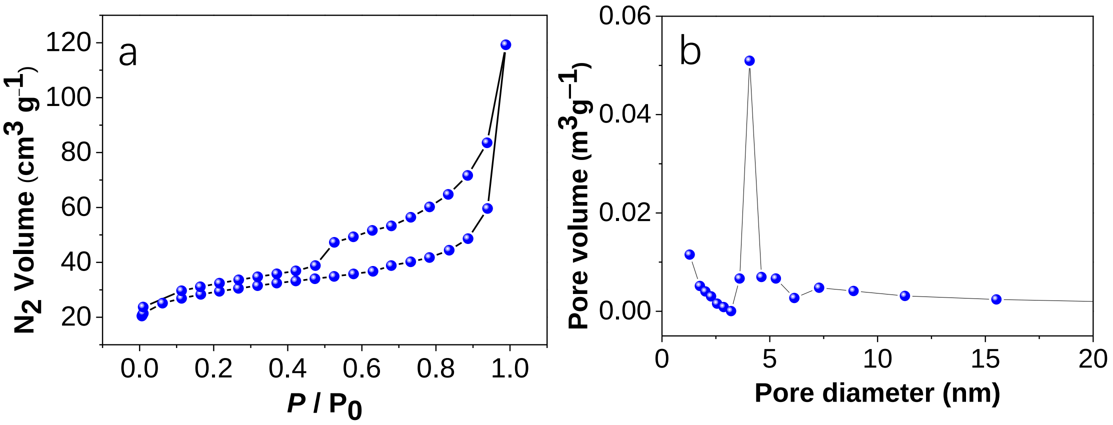

Figure 6. (a) N_2 adsorption/desorption isotherms of the MnO_2/N-C, and (b) pore-size distribution curves for the MnO_2/N-C.

3.2 Electrochemical characterization of MnO_2/N-C

The MnO_2/N-C nanocomposite demonstrated unique structure and excellent physicochemical properties, which suitable for preparation of electrode materials. Figure 7 shows the galvanostatic charge-discharge (GCD) curves of the Chit-C and MnO_2/N-C electrodes at a current density of 1 A g^{-1}. It can be seen that MnO_2/N-C electrode shows typical feature of pseudocapacitor. The charges can be stored and released quickly at equivalent time, indicating a good reversibility. The discharging time of Chit-C was much shorter than that of MnO_2/N-C, indicating a lower charge storage capability under same conditions.

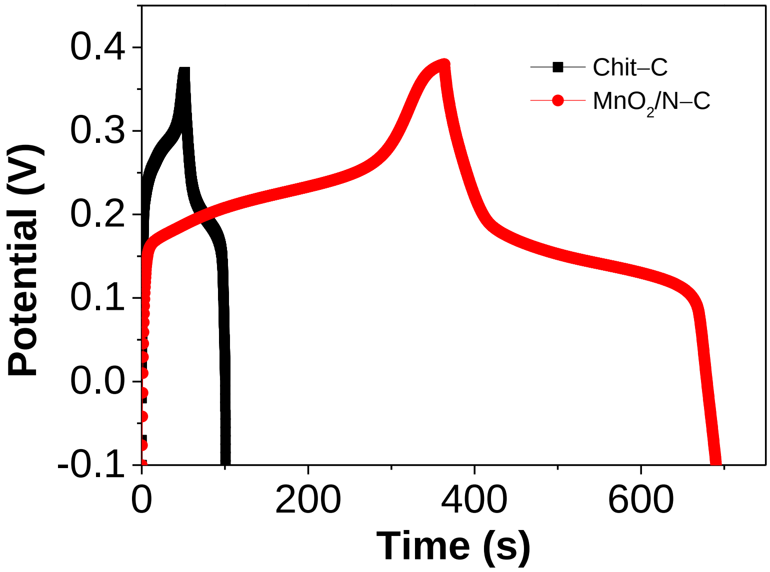

Figure 7. GCD curves of the MnO_2/N-C and Chit-C electrodes recorded at 1 A g^{-1}.

The capacitances were 340.1 and 56.4 F/g for MnO_2/N-C and ZIF-C, respectively. The capacitance of MnO_2/N-C electrode is more than 5 times higher than that of Chit-C, which indicates that the doping of MnO_2 dramatically improve the electrochemical performance of MnO_2/N-C nanocomposite. The possible reason is that MnO_2 enable the formation of graphitic carbon and increase the specific surface area due to the spacer effect, while the carbon substrate facilitates the electron transfer of MnO_2 and improve the stability of the metal oxide, demonstrating synergistic effect between the MnO_2 nanoparticles and the porous carbon substrate. Furthermore, the doping of N in the carbon backbone also contributes the pseudocapacitance [43-46]. The specific capacitance of MnO_2/N-C prepared in this work is also comparable with the reported MnO_2-based materials (Table 1), demonstrating outstanding electrochemical performance.

Table 1. Comparison of specific capacitance of MnO_2/N-C with previous MnO_2 based materials

Sample	Current density ($A\ g^{-1}$)	Specific capacitance ($F\ g^{-1}$)	Reference
CNF-MnO_2/PPy	1	315.8	[1]
α-MnO_2	0.3	311.52	[14]
MnO_2/SC	0.5	231	[47]
MnO_2/rGO	0.1	234.8	[48]
Mn_3O_4/MnO_2	0.5	739	[49]
MnO_2/N-rGO	0.2	368.3	[15]
Fe-doped MnO_2	1	627.3	[50]
MnO_2/g-C_3N_4@PPy NC	2	274	[51]
MnO_2/N-C	1	340.1	This work

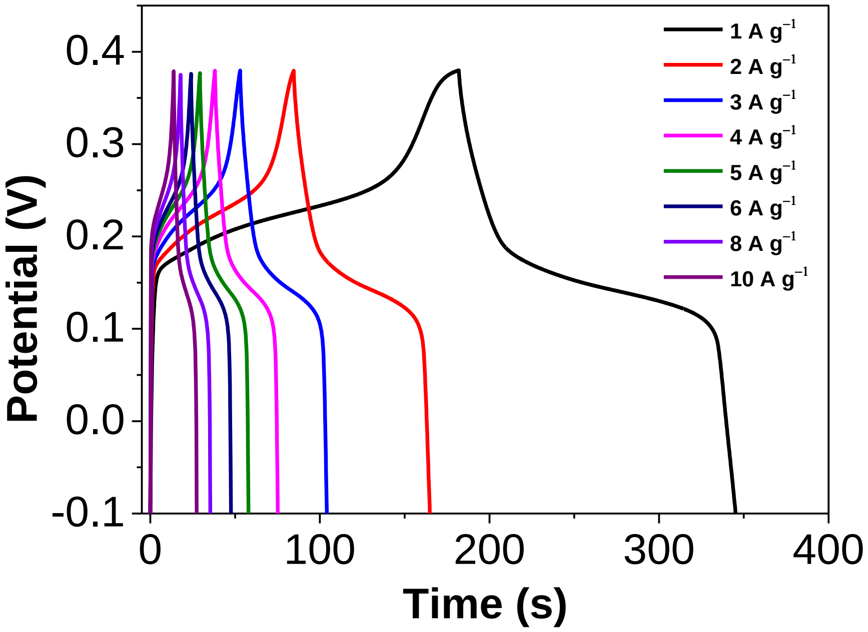

Figure 8. GCD curves of the MnO_2/N-C at the different density of 1, 2, 3, 4, 5, 6, 7, 8 and 10 A/g.

Figure 8 shows the MnO_2/N-C electrode GCD curve of MnO_2/N-C at different current density. The capacitance of MnO_2/N-C decreased from 340.1 and 270.2 F g^{-1} when current densities increased from 1 to 10 A g^{-1}, representing 83.3% retention of the initial capacitance, indicating good high-rate capacitance retention.

The CVs of MnO_2/N-C at various scan rates are shown in Figure 9. There is one couple of redox peaks located at ～ 0.2 V in the CV curves, indicating a faradaic redox reaction behavior. When increasing the scan rates from 5 to 50 mV s^{-1}, the peak current densities increased accordingly. The shape of the CV curves can be well retained, indicating good electrochemical performance and high-rate capability [52, 53].

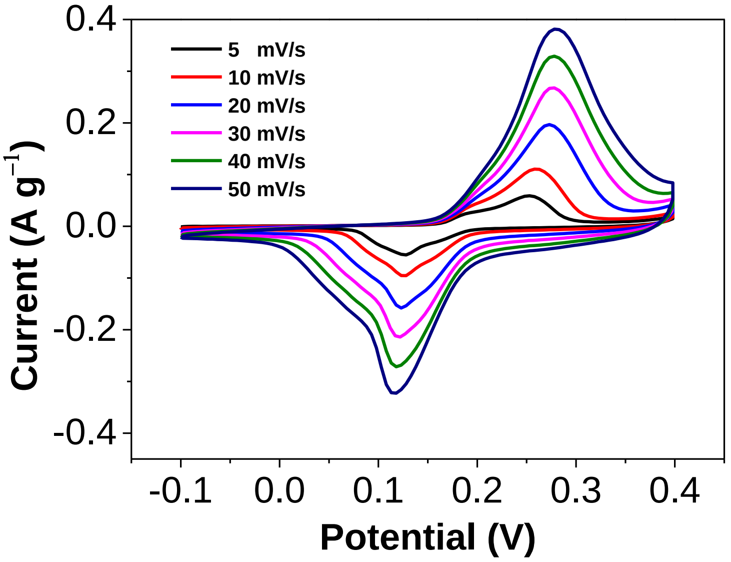

Figure 9. CV curves of the MnO_2/N-C recorded at different scan rates.

The cycling stability of the MnO_2/N-C electrode was studied by charging-discharging cell for 3000 cycles at the current density of 1 A g^{-1}. As shown in Figure 10, the capacitance of the MnO_2/N-C electrode tended to be stable after 500 cycles. After 3000 cycles, the capacitance can be retained 87.6% of its initial capacitance, demonstrating high electrochemical stability.

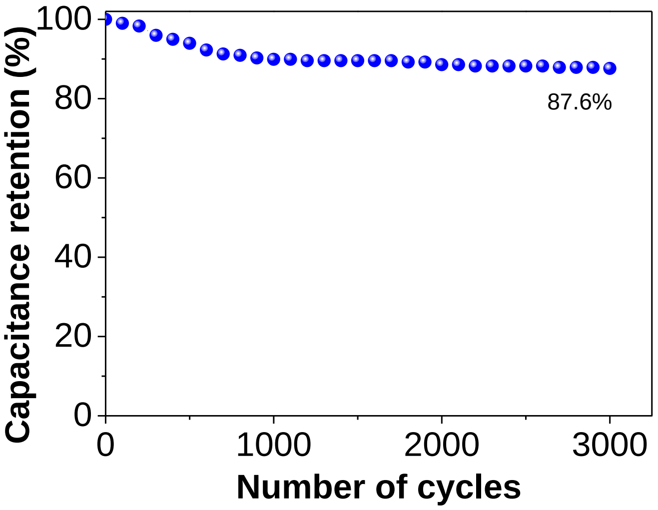

Figure 10. Cycling stability of the MnO_2/N-C supercapacitor recorded at 1 A g^{-1}.

4. CONCLUSIONS

In summary, ultrafine MnO_2 nanoparticles dispersed nitrogen-doped porous carbons was successfully synthesized using one-step carbonization approach. The specific capacitance of the composites is as high as 340.1 F g^{-1} (1 A g^{-1}). A specific capacitance of 270.2 F g^{-1} can be retained at a high current density of 10 A g^{-1}. Furthermore, the MnO_2/N-C sample shows ~87.6% capacitance retention after 3000 charge-discharge cycles. The excellent electrochemical performance of MnO_2/N-C can be attributed to the synergistic effect between the MnO_2 and the carbon substrate.

ACKNOWLEDGEMENTS
This work was supported by the Guangxi undergraduate innovation and entrepreneurship training program (201810595016) and GXNSF (2016GXNSFFA380012, AD17195073, 2017GXNSFDA198018).

References

1. M.A.A.M. Abdah, N.M.M.A. Edris, S. Kulandaivalu, N.A. Rahman, Y. Sulaiman, *Int. J. Hydrogen Energy*, 43 (2018) 17328-17337.
2. Z. Deng, Q. Yi, Y. Zhang, H. Nie, *J. Electroanal. Chem.*, 803 (2017) 95-103.
3. B. Liao, W. Wang, P. Long, X. Deng, B. He, Q. Liu, S. Yi, *Carbon*, 91 (2015) 30-37.
4. B. Liao, P. Long, B. He, S. Yi, Q. Liu, R. Wang, *Carbon*, 73 (2014) 155-162.
5. S. Chen, S. Liu, A. Wen, J. Zhang, H. Nie, J. Chen, R. Zeng, Y. Long, Y. Jin, R. Mai, *Electrochim. Acta*, 271 (2018) 312-318.
6. K. Deng, J. Zhou, X. Li, *Electrochim. Acta*, 114 (2013) 341-346.
7. X. Zhao, S. Zhang, J. Yan, L. Li, G. Wu, W. Shi, G. Yang, N. Guan, P. Cheng, *Inorg. Chem.*, 57 (2018) 5030-5037.
8. J. Xu, A.R. Wilson, A.R. Rathmell, J. Howe, M. Chi, B.J. Wiley, *ACS Nano*, 5 (2011) 6119-6127.
9. Y. Zhang, Q. Yi, Z. Deng, X. Zhou, H. Nie, *Catal. Lett.*, 148 (2018) 1190-1201.
10. K. Deng, C. Li, X. Qiu, J. Zhou, Z. Hou, *Electrochim. Acta*, 174 (2015) 1096-1103.
11. G.R. Xu, Y. Wen, X.P. Min, W.H. Dong, A.P. Tang, H.S. Song, *Electrochim. Acta*, 186 (2015) 133-141.
12. Q. Yi, H. Chu, M. Tang, Y. Zhang, X. Liu, Z. Zhou, H. Nie, *Fuel Cells*, 14 (2014) 827-833.
13. C. An, W. Li, M. Wang, Q. Deng, Y. Wang, *Electrochim. Acta*, 283 (2018) 603-610.
14. X. Bai, X. Tong, Y. Gao, W. Zhu, C. Fu, J. Ma, T. Tan, C. Wang, Y. Luo, H. Sun, *Electrochim. Acta*, 281 (2018) 525-533.
15. X. Feng, Y. Li, G. Chen, Z. Liu, X. Ning, A. Hu, Q. Tang, X. Chen, *Mater. Lett.*, 231 (2018) 114-118.
16. P. Liu, Y. Zhu, X. Gao, Y. Huang, Y. Wang, S. Qin, Y. Zhang, *Chem. Eng. J.*, 350 (2018) 79-88.
17. X. Zhang, J. Xu, H. Wang, J. Zhang, H. Yan, B. Pan, J. Zhou, Y. Xie, *Angew. Chem. Int. Ed.*, 52 (2013) 4361-4365.
18. J. Liu, C. Zhang, T.W. Rees, L. Ke, L. Ji, H. Chao, *Coordin. Chem. Rev.*, 363 (2018) 17-28.
19. S. Zhang, W. Shi, P. Cheng, *Coordin. Chem. Rev.*, 352 (2017) 108-150.
20. J. Yin, G.C. Zhu, B.L. Deng, *Desalination*, 379 (2016) 93-101.
21. Q. Yi, H. Chu, Q. Chen, Z. Yang, X. Liu, Electroanal., 27 (2015) 388-397.
22. Y. Zheng, L. Zhang, P. He, D. Dang, Q. Zeng, J. Zeng, M. Liu, *Electrocatal.*, 9 (2018) 495-504.
23. Z.L. Deng, Q.F. Yi, G. Li, Y. Chen, X.K. Yang, H.D. Nie, *Electrochim. Acta*, 279 (2018) 1-9.
24. Y. Zou, C. Cai, C. Xiang, P. Huang, H. Chu, Z. She, F. Xu, L. Sun, H.B. Kraatz, *Electrochim. Acta*, 261 (2018) 537-547.

25. A. Kumar, D. Sarkar, S. Mukherjee, S. Patil, D.D. Sarma, A. Shukla, *ACS Appl. Mater. Interfaces*, 10 (2018) 42484-42493.
26. X.Y. Yu, L. Deng, B. Zheng, B.R. Zeng, P. Yi, X. Xu, *Dalton T.*, 43 (2014) 1524-1533.
27. M. Tang, Y. Yang, S. Zhang, J. Chen, J. Zhang, Z. Zhou, Q. Liu, *Inorg. Chem.*, 57 (2018) 277-287.
28. S. Zhang, H. Li, E. Duan, Z. Han, L. Li, J. Tang, W. Shi, P. Cheng, *Inorg. Chem.*, 55 (2016) 1202-1207.
29. B. Zheng, R. Yun, J. Bai, Z. Lu, L. Du, Y. Li, *Inorg. Chem.*, 52 (2013) 2823-2829.
30. X. Xia, Y. Long, J. Wang, *Anal. Chim. Acta*, 772 (2013) 81-86.
31. Q. Yi, Q. Chen, *Electrochim. Acta*, 182 (2015) 96-103.
32. J. Tang, W. Gong, T. Cai, T. Xie, C. Deng, Z. Peng, Q. Deng, *RSC Adv.*, 3 (2013) 2543-2547.
33. Q. Yi, Y. Zhang, X. Liu, Y. Yang, *Sci. Chi. Chem.*, 57 (2014) 739-747.
34. R.B. Li, L.L. Yu, S. Li, J. Fan, R. Luo, J.T. Zhao, *Electrochim. Acta*, 284 (2018) 52-59.
35. H. Peng, Z. Mo, S. Liao, H. Liang, L. Yang, F. Luo, H. Song, Y. Zhong, B. Zhang, *Sci. Rep.*, 3 (2013).
36. Z. Wang, B. Zheng, H. Liu, X. Lin, X. Yu, P. Yi, R. Yun, *Cryst. Growth Des.*, 13 (2013) 5001-5006.
37. L. Bao, B. Liu, X. Li, C. Pan, Y. Xie, X. Lu, *Dalton T.*, 45 (2016) 11606-11610.
38. Z. Wang, B. Zheng, H. Liu, P. Yi, X. Li, X. Yu, R. Yun, *Dalton T.*, 42 (2013) 11304-11311.
39. Q. Yi, L. Li, W. Yu, Z. Zhou, G. Xu, *J. Mol. Catal. A-Chem.*, 295 (2008) 34-38.
40. Q. Yu, Z. Shi, X. Liu, S. Luo, W. Wei, *J. Electroanal. Chem.*, 655 (2011) 92-95.
41. Q. Yi, W. Yu, *J. Electroanal. Chem.*, 633 (2009) 159-164.
42. Q. Yi, H. Chu, M. Tang, Z. Yang, Q. Chen, X. Liu, *J. Electroanal. Chem.*, 739 (2015) 178-186.
43. S. Chen, L. Zhang, Y. Long, F. Zhou, *Electroanal.*, 26 (2014) 1236-1248.
44. H. Song, A. Tang, G. Xu, L. Liu, M. Yin, Y. Pan, *Int. J. Electrochem. Sci.*, 13 (2018) 4720-4730.
45. K. Deng, C. Li, X. Qiu, J. Zhou, Z. Hou, *J. Electroanal. Chem.*, 755 (2015) 197-202.
46. J. Chen, Y. Li, K. Lv, W. Zhong, H. Wang, Z. Wu, P. Yi, J. Jiang, *Sens. Actuators B Chem.*, 224 (2016) 298-306.
47. X.P. Chen, J. Wen, C.X. Zhao, Y.T. Li, N. Wang, *Chemistryselect*, 3 (2018) 9301-9307.
48. Y. Chen, J. Zhang, M. Li, C. Yang, L. Zhang, C. Wang, H. Lu, *Electrochim. Acta*, 292 (2018) 115-124.
49. M. Cui, S. Tang, Y. Ma, X. Shi, J.A. Syed, X. Meng, *J. Power Sources*, 396 (2018) 483-490.
50. Q. Gao, J. Wang, B. Ke, J. Wang, Y. Li, *Ceram. Int.*, 44 (2018) 18770-18775.
51. S. Sun, L. Guo, X. Chang, Y. Yu, X. Zhai, *Mater.Lett.*, 236 (2019) 558-561.
52. C.R. Tan, Z.H. Su, B.G. Lin, H.W. Huang, Y.L. Zeng, S. Li, H. Huang, Y.-J. Wang, C.X. Li, G.L. Shen, R.Q. Yu, *Anal. Chimica Acta*, 678 (2010) 203-207.
53. H. Huang, X. Liu, T. Hu, P.K. Chu, *Biosens. Bioelectron.*, 25 (2010) 2078-2083.